Lithium superoxide encapsulated in a benzoquinone anion matrix

Lithium superoxide encapsulated in a benzoquinone anion matrix

Matthew Nava[a,b], Shiyu Zhang[a,1], Katharine S. Pastore[c], Xiaowen Feng[b], Kyle M. Lancaster[c], Daniel G. Nocera[b,2], and Christopher C. Cummins[a,2]

[a]Department of Chemistry, Massachusetts Institute of Technology, Cambridge, MA 02139-4307; [b]Department of Chemistry and Chemical Biology, Harvard University, Cambridge, MA 02138; and [c]Department of Chemistry and Chemical Biology, Cornell University, Ithaca, NY 14853

Contributed by Christopher C. Cummins, October 20, 2021 (sent for review September 14, 2020; reviewed by Larry Curtiss and Stefan A. Freunberger)

Lithium peroxide is the crucial storage material in lithium–air batteries. Understanding the redox properties of this salt is paramount toward improving the performance of this class of batteries. Lithium peroxide, upon exposure to *p*–benzoquinone (*p*–$C_6H_4O_2$) vapor, develops a deep blue color. This blue powder can be formally described as $[Li_2O_2]_{0.3} \cdot [LiO_2]_{0.7} \cdot \{Li[p\text{–}C_6H_4O_2]\}_{0.7}$, though spectroscopic characterization indicates a more nuanced structural speciation. Infrared, Raman, electron paramagnetic resonance, diffuse-reflectance ultraviolet-visible and X-ray absorption spectroscopy reveal that the lithium salt of the benzoquinone radical anion forms on the surface of the lithium peroxide, indicating the occurrence of electron and lithium ion transfer in the solid state. As a result, obligate lithium superoxide is formed and encapsulated in a shell of $Li[p\text{–}C_6H_4O_2]$ with a core of Li_2O_2. Lithium superoxide has been proposed as a critical intermediate in the charge/discharge cycle of Li–air batteries, but has yet to be isolated, owing to instability. The results reported herein provide a snapshot of lithium peroxide/superoxide chemistry in the solid state with redox mediation.

batteries | lithium superoxide | metastable

The advent of metal–air batteries has provided an impetus for understanding the structure, spectroscopic properties, and chemical reactivity of various metal oxides. Lithium–air batteries, which possess a theoretical energy density approaching that of liquid fuels, have emerged as potential candidates to replace lithium-ion batteries (1–4). Lithium–air batteries operate by electron transfer from a high-surface-area cathode to oxygen gas during discharge, generating lithium peroxide deposits. Upon charging, the lithium peroxide is oxidized back to oxygen gas. Despite demonstrating promise as a replacement for lithium-ion batteries, this electrochemical energy-storage system suffers from numerous challenges that must be overcome (5–8), the most important of which is reversible charging.

Lithium superoxide, LiO_2, is an important intermediate in both the reduction of oxygen to lithium peroxide and oxidation of lithium peroxide back to oxygen (9–13). Lithium superoxide, via disproportionation, is thought to be responsible for the growth of large lithium peroxide toroids commonly observed during discharge of nonaqueous lithium–air cells, but is also implicated in numerous studies (14–18) as being responsible, either directly or through the intermediacy of $^1O_2$ (19, 20), for the degradation of the organic solvent and electrolyte in the battery. Furthermore, "superoxide-like" sites on the surface of lithium peroxide are thought to be responsible for both enhanced reactivity with electrolytes in lithium–air batteries and enhanced conductivity (21, 22).

While the superoxide salts of cesium, rubidium, potassium, and sodium are well known, and potassium superoxide is commercially available, the lithium salt of superoxide was not observed definitively until recently in noble gas matrices at low temperatures (23–27). Matrix isolation studies have demonstrated that the infrared (IR) absorption peak associated with the O–O stretch of superoxide loses ∼80% of its intensity when warmed from 15 to 34 K. Two additional reports of the cryogenic preparation of LiO_2 exist: one with O_3 and Li_2O_2 in freon at −65 °C (28) and another involving treatment of O_2 with lithium metal in NH_3 at −78 °C (29).

Strides have also been made toward observing or directly stabilizing lithium superoxide in lithium–air batteries (30–32). At room temperature, lithium superoxide, if unstabilized, is expected to have a fleeting existence, prompting a study to experimentally demonstrate that Raman signals assigned to lithium superoxide in earlier lithium–air works may be ascribed to polyvinylidene fluoride (PVDF) binder that has undergone a dehydrohalogenation reaction (33). However, a subsequent report has asserted that rigorous drying of the PVDF binder precludes the dehydrohalogenation reaction (34). Indeed, the presence and involvement of observable lithium superoxide in lithium–air batteries remains a topic of interest and some controversy (35).

The continued advancement of lithium–air batteries will require improved characterization and understanding of the properties of lithium superoxide, particularly with respect to elucidating the fundamental properties of the salt in the solid state. Reported herein is a solid-state material that models the oxidation of lithium peroxide to lithium superoxide, with a surface coating of *p*–benzoquinone acting as the electron acceptor.

Significance

Lithium superoxide (LiO_2) is an important intermediate in lithium–air batteries, a promising next-generation energy-storage platform. The conductivity, stability, and reactivity profiles of LiO_2 are thought to play a crucial role in the cyclability of lithium–air batteries. We demonstrate that physical encapsulation of Li_2O_2 with an appropriate redox-active molecule may be a viable strategy to access and stabilize LiO_2 at room temperature while simultaneously protecting the solvent and electrolyte from deleterious reactivity derived from LiO_2. Encapsulation with a redox mediator does not impede interfacial electron and lithium-ion transport and provides researchers with a model system that recapitulates the charging of a lithium–air cell.

Author contributions: M.N., S.Z., D.G.N., and C.C.C. designed research; M.N. and S.Z. performed research; M.N., S.Z., K.S.P., and X.F. contributed new reagents/analytic tools; M.N., S.Z., K.S.P., D.G.N., and C.C.C. analyzed data; and M.N., D.G.N., and C.C.C. wrote the paper.

Reviewers: L.C., Argonne National Laboratory; and S.A.F., Institute of Science and Technology Austria.

The authors declare no competing interest.

[1]Present address: Department of Chemistry and Biochemistry, The Ohio State University, Columbus, OH 43210.

[2]To whom correspondence may be addressed. Email: ccummins@mit.edu or dnocera@fas.harvard.edu.

This article contains supporting information online at https://www.pnas.org/lookup/suppl/doi:10.1073/pnas.2019392118/-/DCSupplemental.

Published December 13, 2021.

Fig. 1. The vapor-diffusion setup used to prepare $[Li_2O_2]_{0.3} \cdot [LiO_2]_{0.7} \cdot \{Li[p\text{–}C_6H_4O_2]\}_{0.7}$. The setup consists of a small vial that contains Li_2O_2 sealed within a larger vial containing p–$C_6H_4O_2$. The vial on the left is a freshly prepared sample, while the vial on the right has been allowed to stand at room temperature for a month.

The system recapitulates the proposal of superoxide-like sites on the surface of lithium peroxide in lithium–air batteries.

Results

Synthesis. Lithium peroxide was oxidized by p–benzoquinone (p–$C_6H_4O_2$) using a setup similar to that of growing crystals with two organic solvents (Fig. 1). Vapor diffusion of p–$C_6H_4O_2$ (vapor pressure = 0.1 mm Hg at 25 °C) (36) onto solid lithium peroxide resulted in a gradual color change initially to very faint blue, followed by considerable darkening over the course of several weeks to furnish a sample that ultimately appeared black. This material, designated as compound **1**, was thermodynamically unstable and detonated upon scratching with a metal spatula presumably releasing oxygen (caution: handle with care and in small amounts); for this reason, use of a plastic spatula was preferred.

To accelerate the diffusion of p–$C_6H_4O_2$ onto Li_2O_2, these reactants were placed together as solids into a sealed ampule and heated at 70 °C under a slight vacuum overnight to produce the identical black color, as observed for the material prepared via the vapor-diffusion method. Comparison of the spectroscopic data for **1** (vide infra) produced by these two different methods established the materials to be identical. Sampling by gas chromatography (GC), the headspace gases generated, if any, when using the accelerated ampule synthesis method showed that oxygen gas was not evolved.

Phenylboronic acid is easily oxidized to phenol by hydrogen peroxide generated in situ by hydrolysis of either peroxide or superoxide salts (37). Aqueous titration of **1** with phenylboronic acid gave nearly quantitative conversion to phenol, as verified by NMR spectroscopy (*SI Appendix*, Fig. S1). This result confirms that the O–O bonds remains intact in **1** and reinforces the conclusion that a negligible amount of O_2 gas is released during the formation of **1**.

Curiously, using an equimolar ratio of Li_2O_2 and p–$C_6H_4O_2$ in a sealed ampule to produce **1** consistently resulted in small amounts of p–$C_6H_4O_2$ that were observed to sublime to the top of the ampule, indicating that the molar ratio of Li_2O_2 and p–$C_6H_4O_2$ is not 1:1 in compound **1**. The chemical formula of **1**, as determined by C and H elemental analysis, indicated limiting detailed formulations of either $[Li_2O_2]_{0.3} \cdot [LiO_2]_{0.7} \cdot \{Li[p\text{–}C_6H_4O_2]\}_{0.7}$ or $[Li_2O_2] \cdot [p\text{–}C_6H_4O_2]_{0.7}$. Furthermore, unconsumed p–$C_6H_4O_2$ can be recovered from the 1:1 reaction in quantities consistent with our established chemical formula of **1**. Running the synthesis of **1** using an excess of p–$C_6H_4O_2$ also did not result in fractional compositions of p–$C_6H_4O_2$ exceeding 0.7, as the excess p–$C_6H_4O_2$ was recovered following its sublimation from the black solid sample of **1**.

Examination of **1** by scanning electron microscopy (SEM; Fig. 2) revealed distinct morphological changes as compared with the Li_2O_2 starting material. Commercial Li_2O_2, as purchased, is composed of particles several hundred nanometers in diameter. Upon exposure of Li_2O_2 to p–$C_6H_4O_2$, fusing of particles was observed, suggesting that the black material that formed on the outer surface of the peroxide causes the particles to coalesce (Fig. 2 and *SI Appendix*, Fig. S2).

The blue color of quinone monoanions (38, 39) prompted us to independently prepare $Li[p\text{–}C_6H_4O_2]$ (**2**) to determine whether the benzoquinone anion radical is responsible for the black color of **1**. As the lithium salt of the dianion, $Li_2[p\text{–}C_6H_4O_2]$, is known, a comproportionation strategy was pursued. Using the vapor-diffusion method, it was found that **2** could be prepared from $Li_2[p\text{–}C_6H_4O_2]$ and p–$C_6H_4O_2$ as an intense blue powder. Salt **2** could also be prepared via mechanical mixing of $Li_2[p\text{–}C_6H_4O_2]$ and p–$C_6H_4O_2$ in a mortar and pestle. Vapor diffusion or

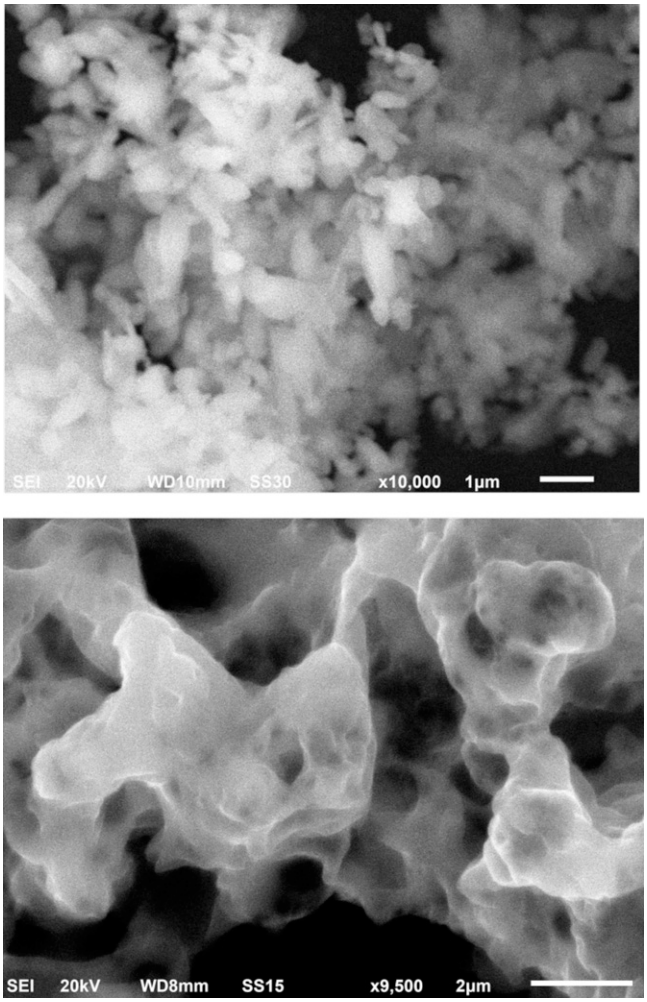

Fig. 2. SEM images of commercial Li_2O_2 (*Upper*) and **1** (*Lower*). Fusing of the Li_2O_2 particles is evident in **1**.

mechanical mixing gave samples of **2** having indistinguishable properties, with the latter method better suited for producing larger quantities of the salt. When samples of **2** were heated above 70 °C and under vacuum, the disproportionation reaction prevailed to furnish $Li_2[p\text{–}C_6H_4O_2]$ (*SI Appendix*, Figs. S3 and S4). Hence, the successful synthesis of **1** from Li_2O_2 and $p\text{–}C_6H_4O_2$ (vide supra) was achieved for temperatures at or below 70 °C.

Fig. 3 displays overlaid, separately acquired cyclic voltammograms for the reduction of O_2 and $p\text{–}C_6H_4O_2$ in dimethylformamide (DMF) with tetrabutylammonium ([TBA]) hexafluorophosphate electrolyte. The irreversible electrochemistry of oxygen and quinone associated with lithium cations was avoided with $[TBA]PF_6$ supporting electrolyte, but such a substitution resulted in an approximately several-hundred-millivolt cathodic shift relative to their lithium potentials (40, 41). $p\text{–}C_6H_4O_2$ has two reversible reductions corresponding to the 0/– and –/2– couples at −0.67 V and −1.42 V vs. Ag/Ag^+. The reduction of oxygen to superoxide fell between the two reduction potentials of the quinone at −1.02 V vs. Ag/Ag^+.

Spectroscopy. Fig. 4 displays the diffuse reflectance ultraviolet-visible (UV-vis) spectrum of **1**. The visible spectral region is dominated by a pronounced absorption band with λ_{max} = 825 nm, accounting for the blue color of the compound. Salt **2**, prepared by mechanical grinding, exhibits an identical absorption band. The only notable difference between the absorption profiles of **1** and **2** is that the former spectrum exhibits a more pronounced shoulder at λ = 250 nm; superoxide exhibits an absorption at this wavelength (42).

Electron paramagnetic resonance (EPR) spectra of **1** and **2** (Fig. 5) display a single broad signal centered at g = 2.008, a feature consistent with the presence of a spin one-half organic radical. Hyperfine coupling could not be resolved at 77 K or by dilution of the samples with sodium sulfate due to the close intermolecular contact of the spin-bearing species composing both samples (vide infra). EPR spin quantification, a method used to determine the number of radicals present in a bulk sample, was performed by spin integration of **2** against an EPR quantification standard 2,2-diphenyl-1-picrylhydrazyl and indicated the spin yield (the ratio of the number of observed spins against the expected number of spins) of **2** to be 2.4% (*SI Appendix*, Fig. S5).

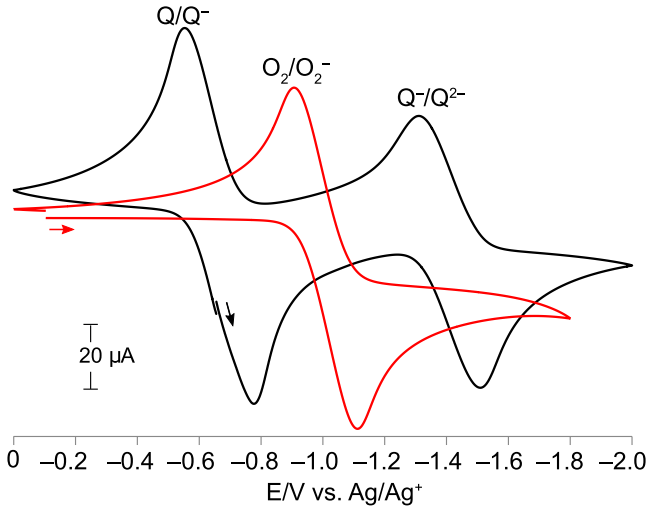

Fig. 3. Cyclic voltammograms of $p\text{–}C_6H_4O_2$ (Q) at 4.8 mM (black trace) and saturated O_2 (red trace) in DMF with $[TBA]PF_6$ supporting electrolyte. The working electrode was a glassy carbon button electrode, paired with a platinum counter electrode and a Ag/Ag^+ reference electrode. Scan rate = 20 mV/s. The superoxide/peroxide couple is omitted due to its irreversible nature.

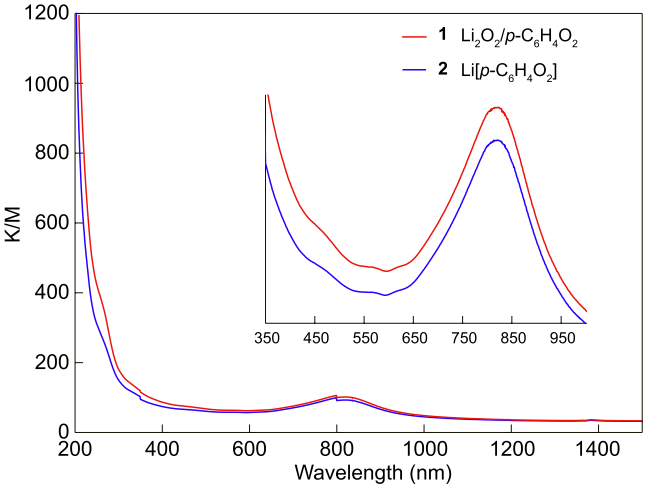

Fig. 4. Diffuse reflectance UV-vis spectra of **1** (red) and **2** (blue). *Inset* is corrected for a light source change of the UV-vis spectrophotometer at 800 nm.

A broad EPR signal derived from a powdered sample of the alkali quinone radical anion $Na[o\text{–}C_6Cl_4O_2]$ has been observed (43), and similar spin yields (0.1 to 10%) have been measured for quinone radical anions (44). A noteworthy feature of the EPR spectrum of **1**, although not always as pronounced, is the presence of an additional narrow line at g = 2.009. Powdered potassium superoxide exhibits a similarly narrow line in its EPR spectrum (45). The presence of superoxide in **1**, as suggested by the EPR data, is further supported by superconducting quantum interference device magnetometry. Subtraction of the direct current susceptibility of **2** from that of **1** (mass-corrected; *SI Appendix*, Fig. S6) indicates an additional paramagnetic species in **1**, consistent with the presence of superoxide.

IR spectroscopy was used to determine the redox level of the benzoquinone present in **1**. The position of the C=C and C–O IR stretches of quinones are sensitive to the reduction state of the molecule, with red-shifting of the aforementioned vibrations occurring upon reduction of quinone to the quinone radical anion and, finally, to the dianionic phenolate salt. The IR spectrum of **1** is superimposed with that of $p\text{–}C_6H_4O_2$ and $Li_2[p\text{–}C_6H_4O_2]$ in Fig. 6. *p*–benzoquinone has asymmetric and symmetric C=O stretches at 1,670 and 1,646 cm^{-1}, respectively (46). The C=C stretch of *p*–benzoquinone is coupled to the two C=O stretches and is observed at 1,578 cm^{-1}. The C=C stretches of $Li_2[p\text{–}C_6H_4O_2]$ are observed from 1,475 to 1,442 cm^{-1} and the C–O stretch is likely centered at 1,172 cm^{-1}, clearly contrasting with that of *p*–benzoquinone. The C=O and C=C stretches of **1** fall between those of both $p\text{–}C_6H_4O_2$ and $Li_2[p\text{–}C_6H_4O_2]$, with tentative assignments of the C=C stretches at 1,531 cm^{-1} and the C=O stretch at 1,405 cm^{-1}. These values compare favorably with data for spectroelectrochemically generated *p*–benzoquinone radical anion, which has assigned values of 1,506 cm^{-1} and 1,347 cm^{-1} for the C=C and C=O stretches, respectively (47). Broad bands associated with the Li–O stretches of Li_2O_2 are observed in the IR spectrum of **1** below 600 cm^{-1} (*SI Appendix*, Fig. S7*A*).

The resonance Raman spectrum of **1** is overlaid with that of **2** in Fig. 7. The spectra of **1** and **2** are nearly identical and are consonant with that reported for *p*–benzoquinone radical anion in solution (47). Comparison of the Raman spectrum of **2** with that of $p\text{–}C_6H_4O_2$ and $Li_2[p\text{–}C_6H_4O_2]$ supports the notion that the redox level of **2** is that of a monoanion (*SI Appendix*, Figs. S8 and S9). Noticeably absent from the Raman spectrum of **1** are lines due to Li_2O_2. The strong absorption band of $Li[p\text{–}C_6H_4O_2]$ at 825 nm results in attenuation of

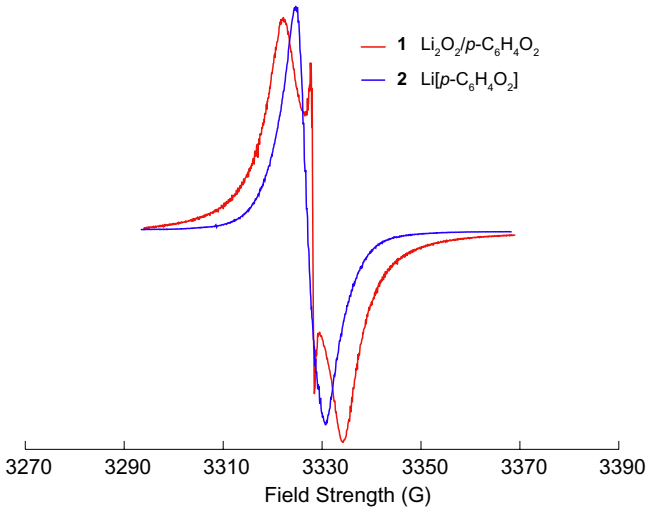

Fig. 5. EPR spectra of **1** and **2** collected at 77 K.

the 785-nm Raman excitation light below the surface of the particles of **1**. Accordingly, only the surface of **1** is resonance-enhanced, and, as a consequence, Li_2O_2 and LiO_2, if present, are not observed. In an effort to break apart the light-attenuating surface coating, samples of **1** were gently compressed between microscope slides; however, the Raman spectrum of these crushed samples was identical to that shown in Fig. 7. The inability to readily observe LiO_2 in samples of **1** prompted studies focused on the in situ monitoring of the conversion of Li_2O_2 to **1** (*SI Appendix*, section S3.4). Upon the layering of *p*–benzoquinone on powdered Li_2O_2 in a quartz capillary, a blue gradient developed across the Li_2O_2 (*SI Appendix*, Fig. S10). Raman spectral analysis along this gradient revealed the presence of a weak band at 1,139 cm^{-1} (Fig. 7, *Inset*) superimposed on a highly fluorescent background. This band was not attributable to *p*–benzoquinone or its radical anion (*SI Appendix*, Fig. S11), is in a region typically associated with superoxide O–O stretches (32), and may be that of LiO_2 present in the sample.

Oxygen K-edge (1s → valence) X-ray absorption spectroscopy (XAS) was used to differentiate the natures of oxygen present in **1**. Oxygen K-edge XAS of **1**, **2**, Li_2O_2, and $Li_2[p\text{–}C_6H_4O_2]$ were collected, and the corresponding data are presented in Fig. 8; the fitted peak energies are shown in *SI Appendix*, Fig. S12 and summarized in *SI Appendix*, Table S4. In general, the oxygen K-edge π^* features of C=O are at lower energy than the σ^* features of O–H (48). A detailed report of the electron energy-loss spectra of *p*–benzoquinone, hydroquinone, and phenol gives assignments of these features based on molecular orbital theory (49).

The π^* feature of $p\text{–}C_6H_4O_2$ is at 529.85 eV, and the σ^* feature of OH in hydroquinone is at 534.6 eV. The presence of Li in the bonding environment of Li_2O_2 shifts the σ^* O–O feature to 531.6 eV, which is lower energy as compared to that of H_2O_2. Two peaks of about equal intensity in the spectrum of $Li_2[p\text{–}C_6H_4O_2]$ at 529.9 and 532.6 eV are also in the spectrum of the independently prepared samples of **2** reported here, although the higher energy peak is of much higher relative intensity. If we attribute the first peak to the π^* C=O and the second to σ^* O–Li, since it is shifted by 2 eV from literature σ^* O–H, the data are consistent with formation of the quinone radical in **2**, with some unreacted or reoxidized quinone present. The broad peak in **1** attributed to Li_2O_2 obscures energetically proximate features, if any; however, the fitted peak at 532.3 eV may come from $Li[p\text{–}C_6H_4O_2]$, as supported by the comparison with the genuine spectrum of **2**.

Powder X-Ray Diffraction (PXRD). The PXRD pattern of **1** is shown in Fig. 9. The pattern is a composite of contributions from **2** (blue bars) and Li_2O_2 (orange bars). The peaks of **1** labeled with blue bars in Fig. 9 coincide with the PXRD pattern of an independently prepared sample of authentic **2** (*SI Appendix*, Fig. S13*D*). *SI Appendix*, Fig. S13*C* displays a comparison of the PXRD patterns of **2** to $Li_2[p\text{–}C_6H_4O_2]$; none of the PXRD peaks of $Li_2[p\text{–}C_6H_4O_2]$ (50) are observed in samples of **1**. The majority of the diffraction peaks in **1** coincide with those of **2** or Li_2O_2; the presence of both these species in **1** is consistent with the formulation of $[Li_2O_2]_{0.3} \cdot [LiO_2]_{0.7} \cdot \{Li[p\text{–}C_6H_4O_2]\}_{0.7}$. The peaks labeled with asterisks in Fig. 9 are of unknown origin, but could be posited tentatively to arise from LiO_2.

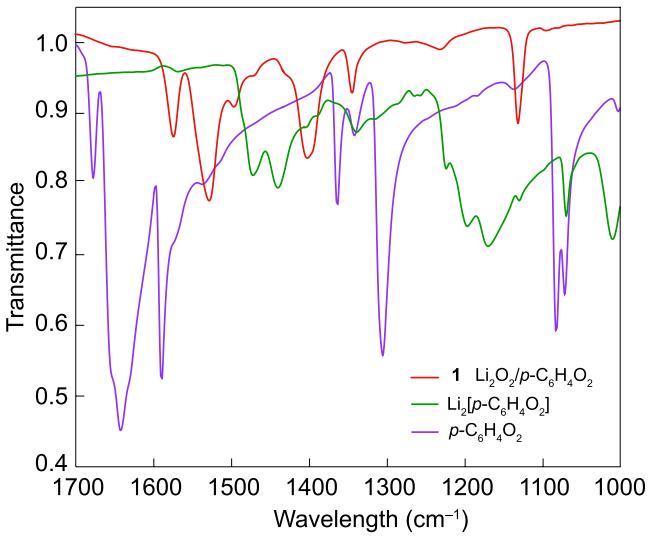

Fig. 6. Attenuated total reflectance-IR spectra of **1** (red), $p\text{–}C_6H_4O_2$ (purple), and $Li_2[p\text{–}C_6H_4O_2]$ (green) from 1,000 to 1,700 cm^{-1}.

Discussion

p–benzoquinone, a yellow solid at room temperature, has a high vapor pressure. The surface of lithium peroxide exposed to $p\text{–}C_6H_4O_2$ develops an intense blue color. During the course of this conversion to deliver **1**, the following reactions were considered to occur:

$$Li_2O_2 + p\text{–}C_6H_4O_2 \rightarrow Li_2O_2 \cdot [p\text{–}C_6H_4O_2]_{ads}, \quad [1]$$

$$Li_2O_2 + p\text{–}C_6H_4O_2 \rightarrow LiO_2 + Li[p\text{–}C_6H_4O_2], \quad [2]$$

$$2\,Li_2O_2 + p\text{–}C_6H_4O_2 \rightarrow 2\,LiO_2 + Li_2[p\text{–}C_6H_4O_2], \quad [3]$$

$$Li_2O_2 + 2\,p\text{–}C_6H_4O_2 \rightarrow 2\,Li[p\text{–}C_6H_4O_2] + O_2, \quad [4]$$

$$Li_2O_2 + p\text{–}C_6H_4O_2 \rightarrow Li_2[p\text{–}C_6H_4O_2] + O_2. \quad [5]$$

Reactions 1–5 describe varying degrees of charge transfer from lithium peroxide to benzoquinone. Reaction 1, which depicts the formation of an adsorption layer of benzoquinone on lithium peroxide, may be ruled out on the basis of the color change of $p\text{–}C_6H_4O_2$ from yellow to blue (and ultimately black), which is indicative of reduction of $p\text{–}C_6H_4O_2$. Similarly, reactions 4 and 5 may be dismissed, as analysis of the reaction headspace by GC did not reveal any oxygen production. Moreover, results from the titration of the product with $PhB(OH)_2$ to produce PhOH quantitatively suggest that no O_2 was lost from the sample; the oxygen speciation has an O–O bond of peroxide or superoxide, and peroxide can directly oxidize boronic acids, while superoxide may convert to peroxide upon disproportionation in water (37, 51–53). Additionally, the cyclic voltammograms in Fig. 3 show that it is thermodynamically unfavorable for the radical anion

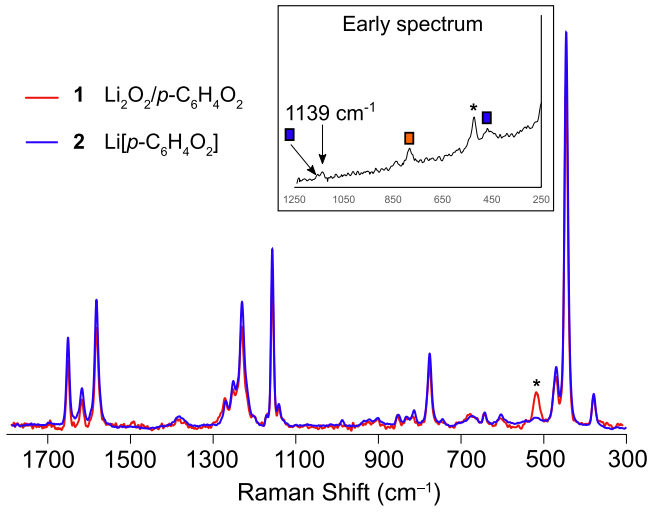

Fig. 7. Raman spectral overlay of **1** (red) and **2** (blue). *Inset* shows a Raman spectrum acquired during the early stages of *p*–benzoquinone vapor absorption on Li_2O_2; a band in the region typically associated with superoxides is observable prior to the formation of an optically thick coating of Li[*p*–$C_6H_4O_2$] on **1**. Asterisks indicate bands associated with quartz capillaries, while boxes above peaks indicate bands associated with Li_2O_2 (orange) or *p*–benzoquinone$^{0/-1}$ (blue).

of *p*–$C_6H_4O_2$ to oxidize superoxide to produce O_2. Reactions 2 and 3 depict electron transfer and lithium-ion diffusion from lithium peroxide to benzoquinone to generate lithium superoxide and either the benzoquinone radical monoanion or dianion, respectively. The spectroscopic properties of **2** rule out reaction 3 and point to reaction 2 as being operative.

The radical monoanion of *p*–$C_6H_4O_2$ has been studied in great detail and can be prepared by a variety of methods, such as pulse radiolysis of the neutral quinone in matrices (54) or frozen solutions (55) or direct reduction of *p*–benzoquinone with potassium in the presence of Kryptofix® 222 or crown ethers in tetrahydrofuran (56). The Li^+ salt of *p*–$C_6H_4O_2$ radical monoanion is less studied, and only a handful of instances detailing the preparation of this compound are known (57–60). We therefore sought to prepare Li[*p*–$C_6H_4O_2$] (**2**) independently. We pursued the solid-state comproportionation reaction of Li_2[*p*–$C_6H_4O_2$], prepared by known methods (50), with *p*–$C_6H_4O_2$ to deliver **2**, as supported by a host of spectroscopic techniques:

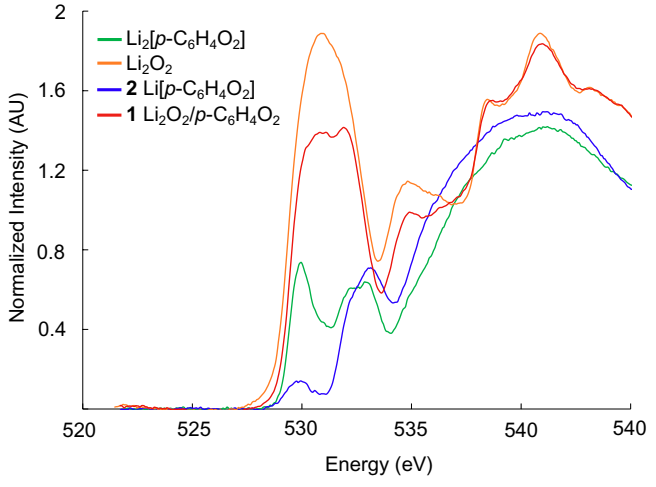

Fig. 8. Overlaid O K-edge XAS spectra of compounds Li_2[*p*–$C_6H_4O_2$], **2**, Li_2O_2, and **1**. AU, arbitrary units.

1) the $S = 1/2$ EPR signal of Fig. 5; 2) the energy of the C=O stretching frequency (in IR and Raman spectra; Figs. 6 and 7) of **2** is intermediate between *p*–$C_6H_4O_2$ and the Li_2[*p*–$C_6H_4O_2$]; and 3) the XAS spectrum of **2** exhibits one major peak in the O 2p K-edge (as opposed to two peaks for the dianion). The viability of driving the comproportionation reaction to produce **2** using mechanical mixing was confirmed by Raman spectroscopy. Comparison of the Raman spectrum of **2** with those of Li_2[*p*–$C_6H_4O_2$] and *p*–$C_6H_4O_2$ (*SI Appendix*, Figs. S8 and S9) demonstrates the formation of Li[*p*–$C_6H_4O_2$] upon mixing.

The UV-vis absorption profile of **1** is strikingly similar to that of **2**. The dark blue color of the two materials is a result of identical absorption bands centered at 825 nm (Fig. 4). This absorbance is strikingly similar to semiquinone radical anions prepared in anhydrous *t*-butanol (57) and reminiscent of that arising from the π dimer exciplex formed upon the reduction of 2,3-dichloro-5,6-dicyano-1,4-benzoquinone (38, 39). In the cases of **1** and **2**, π-stacking between quinone radical anions may be facilitated by lithium counterions bridging the oxygens of neighboring quinone radical anions. The absorption band of weaker intensity at 460 nm in **1** and **2** has been ascribed to the $^2B_{2g} \rightarrow {}^2B_{3u}$ highest occupied molecular orbital-lowest unoccupied molecular orbital electronic transition of benzoquinone radical anion (47, 61). This transition exhibits a strong dependence on the solvent environment, with values of the absorption maximum (max) ranging from 427 nm in water to 454 nm in pyridine. The UV-vis spectrum of both powdered potassium superoxide (45) and superoxide in solution have been reported (42, 62, 63). Superoxide in solution has an absorption max at 250 nm, while solid potassium superoxide's absorption max is 350 nm and tails out to 600 nm. Strong absorptions assigned as Li[*p*–$C_6H_4O_2$] dominate the UV-vis spectrum of **1**; however, small deviations of the spectrum of **1** relative to **2** indicate an additional band at 265 nm that may be that of superoxide.

Other spectroscopic data (resonance Raman, IR, and EPR) point to the presence of **2** as a component of **1**. The Raman spectrum of **1** is overlaid with that of **2** in Fig. 7. The agreement between the spectra confirms that Li[*p*–$C_6H_4O_2$] is present in both samples and has not been chemically altered in **1**. Additionally, Raman spectra taken at time points corresponding to low coverages of **2** on **1** indicate the presence of a species consistent with a superoxide O–O stretch at 1,139 cm^{-1}. The EPR spectra of **1** and **2** are dominated by a broad featureless absorption at $g = 2.008$; however, the spectrum of **1** displays a significantly narrower signal. The superposition of a broad and narrow absorption has been noted for samples of potassium superoxide, with the broad line ascribed to the majority of the strong exchange-coupled superoxide anions present in the sample and the narrow line attributed to a very small population ($\sim$1 in every 10^4 spins) of superoxide anions that are able to freely rotate in the sample and have poor electronic coupling with their environment (45). The EPR spectrum of **1** is dominated by features arising from Li[*p*–$C_6H_4O_2$], but the absence of the narrow absorption in the spectrum of **2** suggests that this feature is unique to **1** and may be tentatively assigned as arising from the superoxide ion. The presence of this feature is not observed uniformly across all preparations of **1**, presumably due to the extremely small percentage of spins contributing to this narrow line. The EPR spectrum of Li[*p*–$C_6H_4O_2$] has been observed in prior work (57, 60), with the notable observation of hyperfine structure when EPR spectra were recorded with dilute samples. Loss of hyperfine structure in spectra of Li[*p*–$C_6H_4O_2$] is seen for concentrated samples (60). The latter observation is consonant with the lack of hyperfine structure seen for solid samples of **1** and **2**.

PXRD analysis lends further support to the assignment of Li[*p*–$C_6H_4O_2$] as a component of **1**. The PXRD pattern of **1** shown in Fig. 9 has peaks coincident with those of **2**

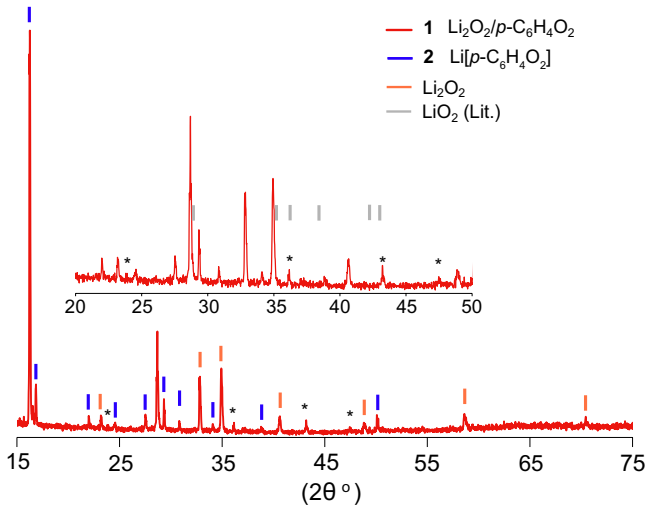

Fig. 9. PXRD pattern of **1** (red). Lithium peroxide and **2** are observed in **1** and are indicated with orange and blue marks, respectively. Several unknown diffraction peaks are marked with asterisks. *Inset* shows a select region of the PXRD pattern along with gray marks indicating the position of peaks that have been previously ascribed to LiO_2 (34). The PXRD was recorded with Ni-filtered Cu-K_α radiation.

prepared by mechanical comproportionation of Li$_2$[p–$C_6H_4O_2$] and p–$C_6H_4O_2$. Remaining peaks present in the pattern of **1** are assigned either to Li_2O_2 or unknown phase(s). Several computational studies have predicted that the lowest-energy structure of LiO_2 is the orthorhombic phase (64–66). Although possible correspondence of the observed pattern with that of a simulated pattern derived from ab initio calculations (64–66) occurs near $2\theta = 35°$, and the peaks labeled by asterisks in Fig. 9 are coincident with peaks assigned as LiO_2 (34), definitive assignment of the unknown peaks cannot be made, nor can it be determined whether LiO_2, if present in **1**, is amorphous.

The O K-edge XAS of **1**, **2**, Li$_2$[p–$C_6H_4O_2$], and Li_2O_2 demonstrate marked differences between the samples. Differentiating features are observed in the spectra of **2** and Li$_2$[p–$C_6H_4O_2$], providing additional evidence for disproportionation of Li$_2$[p–$C_6H_4O_2$] and p–$C_6H_4O_2$. The presence of **2** and Li_2O_2 as a component of **1** obscures the pre-edge region of the O K-edge XAS spectrum of **1**, where LiO_2 has been previously measured in matrices (67), precluding its definitive identification.

The formulation of **1** may be addressed, having established that **1** is composed of Li[p–$C_6H_4O_2$] and Li_2O_2 and inferred the presence of LiO_2 through EPR, PXRD, and titration methods. Elemental analysis of **1** consistently indicates a formula of $[Li_2O_2]\cdot[p\text{–}C_6H_4O_2]_{0.7}$, yet spectroscopic analysis indicates that the redox level of p–$C_6H_4O_2$ is that of a monoanion. To accommodate the redox level of p–benzoquinone, a commensurate number of lithium ions and electrons must be drawn from Li_2O_2. In the context of reaction 2, a more detailed formula of **1** including speciation is proposed to be $[Li_2O_2]_{0.3}\cdot[LiO_2]_{0.7}\cdot\{Li[p\text{–}C_6H_4O_2]\}_{0.7}$. Why Li_2O_2 stops absorbing p–$C_6H_4O_2$ after 0.7 equivalents is currently unknown, but may be related to particle size.

A schematic representation of **1** is provided in Fig. 10. Commercial lithium peroxide is composed of particles with a diameter on the order of several hundred nanometers (Fig. 2). Raman and IR spectroscopy clearly indicate the presence of **2** on the surface of **1**. The Li[p–$C_6H_4O_2$] forms a shell about Li_2O_2 with a thickness of approximately one-quarter of the diameter of the Li_2O_2 particle based upon a density of circa 1.6 g/cm^3 for **2**. Notably, the schematic shown in Fig. 10 resembles that of theoretical models (68) and experimental studies (69, 70), which propose an amorphous LiO_2 shell around a crystalline Li_2O_2 core in nonaqueous Li-O_2 batteries. The lithium peroxide core is believed to be the source of both lithium ions and electrons, resulting in the formation of LiO_2. The shell of Li[p–$C_6H_4O_2$] may be crucial for kinetic stabilization of the thermodynamically unstable LiO_2 layer against disproportionation to Li_2O_2 and O_2. A recent computational and experimental study concluded that interfacial charge transfer from LiO_2 to the electrolyte may be responsible for the observed stability of LiO_2 (66). A degree of charge transfer from LiO_2 to Li[p–$C_6H_4O_2$] in **1** is expected, based upon the reduction potentials of the relevant species presented in Fig. 3, providing a plausible explanation for the resistance of LiO_2 to disproportionation in **1** in addition to physical confinement.

At the center of the particle in Fig. 10, crystalline Li_2O_2 remains and accounts for the substoichometric ratio of p–$C_6H_4O_2$ relative to Li_2O_2. Upon heating above 70 °C, the coating layer of Li[p–$C_6H_4O_2$] disproportionates into Li$_2$[p–$C_6H_4O_2$] and p–$C_6H_4O_2$. An earlier study noted that adding an alkali base to a mixture of p–$C_6H_4O_2$ and hydroquinone (p–$C_6H_4(OH)_2$) resulted in the alkali base developing a blue color, which was believed to be due to trapped benzoquinone radical anions on the surface of the alkali base support (71). This result is particularly interesting because it suggests a strategy to prepare unstable intermediates with adsorption on a reactive support surface, which has been utilized in the present study. In the core–shell structure of **1**, there are two components determining electron and ion conduction throughout the material: the LiO_2 core and a Li[p–$C_6H_4O_2$] shell. With regard to the core, recent experimental (72) and first-principles studies (73–75) have indicated that LiO_2 possesses remarkable ionic and electronic conductivities, greatly exceeding that of other alkali superoxides and peroxides (75), presumably crucial properties necessary to form the structure shown in Fig. 10. The other component of the structure in Fig. 10 is Li[p–$C_6H_4O_2$]. Millimeter-thick films of Li[p–$C_6H_4O_2$] have been previously prepared via electrodeposition of p–$C_6H_4O_2$ from a lithium-ion–containing electrolyte (43). Deposition of

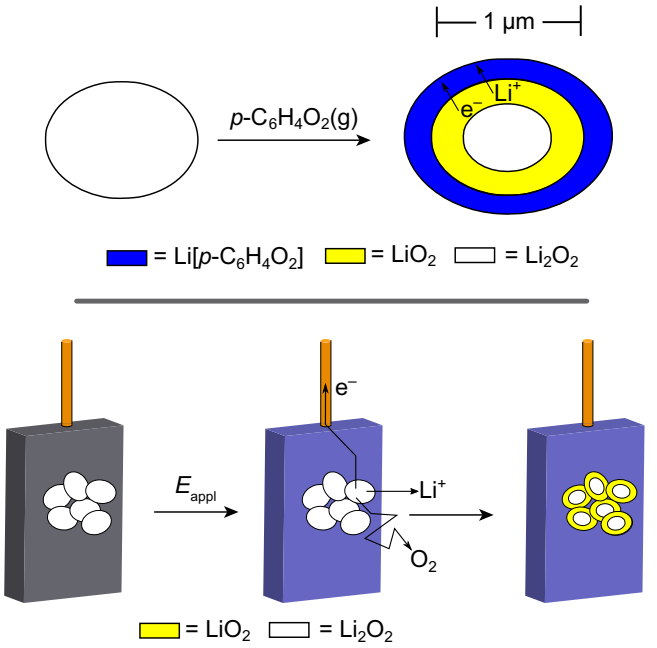

Fig. 10. Schematic representation of **1** (*Upper*) assuming the material starts from a 1 μm sphere of Li_2O_2. The analogy of **1** to a charging electrode is represented in *Lower*.

thick films of Li[p–$C_6H_4O_2$] highlight the excellent conductivity of this material; however, the counterbalancing lithium cation need only be deposited on the surface of the growing film from solution. In contrast, in forming the core–shell structure of **1**, lithium cations must diffuse from the core to the outer surface of the shell. Thus, termination of **1** with a core–shell structure suggests that the lithium-ion mobility of the shell is kinetically limiting. The schematic presented in Fig. 10 along with qualitative observations of the electrical and ionic conductivity of the constituents of **1** may also explain why **1** does not absorb more than 0.7 equivalents of p–$C_6H_4O_2$. At the early stages of the reaction in which **1** is formed from Li_2O_2 and p–$C_6H_4O_2$, the area of the interface between LiO_2 and Li_2O_2 is large, allowing for lithium and electron transfer from Li_2O_2, despite its poor conductivity. However, as the reaction progresses, this interface drastically shrinks in size, and ultimately the rate of the reaction becomes limited by the poor conductivity of Li_2O_2. Additionally, disproportionation of LiO_2 at the Li[p–$C_6H_4O_2$]/Li_2O_2 interface may place a poorly conducting barrier between the quinone and original particle.

Several recent publications have used benzoquinone and anthraquinone derivatives as soluble redox mediators in lithium–air batteries (76). It was found that 2,5-di-*tert*-butyl-1,4-benzoquinone enhances the rate of the oxygen reduction reaction and drastically increases the capacity of a lithium–air cells (77, 78). Another study found that benzoquinone exhibited the best performance as a redox mediator based on cathodic chronopotentiometry, although detection of lithium peroxide via XPS was the sole physical characterization method (79), while another study has suggested an explicit interaction between anthraquinone and LiO_2 in solution (80). Importantly, in the present study, the solvent-free conditions employed enforce physical confinement of the lithium peroxide/superoxide layer, which may be crucial in stabilizing thermodynamically unstable lithium superoxide. This strategy of physical confinement may also be crucial in ameliorating lithium superoxide-induced solvent degradation, a key challenge to overcome if higher cycling numbers are to be achieved in lithium–air batteries (15, 29, 81–83).

Conclusions

Exposure of solid Li_2O_2 to p–$C_6H_4O_2$ results in the formation of a dark black material. This material has been investigated by a variety of spectroscopic methods and is best described as a coating of Li[p–$C_6H_4O_2$] on LiO_2 and Li_2O_2. This reaction is unique in that electron transfer from Li_2O_2 occurs with p–$C_6H_4O_2$, resulting in a comproportionation-like reaction. This reaction methodology can be extended to the preparation of the quinone radical anion from Li_2[p–$C_6H_4O_2$] and p–$C_6H_4O_2$. The preparation of **1** and compounds similar to **1** allow for controlled "snapshots" of lithium peroxide during the electron transfer from Li_2O_2 to electron acceptors (redox shuttles). Indeed, we show here that LiO_2 may be stabilized on Li_2O_2 surfaces in the presence of the electron accepting p–$C_6H_4O_2$, which, as highlighted in Fig. 10, is a surrogate for the anode of a lithium–air battery. By careful control of the potential of the electron acceptor and concentration, it may be possible to intimately study the properties of electron-deficient Li_2O_2, LiO_2 and the superoxide-like sites, which crucially contribute to the conductivity of Li_2O_2. Furthermore, a strategy of molecular encapsulation of Li_2O_2 with a conductive layer may serve as a promising method to protect cell components, including the electrolyte, from deleterious degradation reactions initiated by LiO_2 and by extension improve the performance of metal–air batteries.

Supporting Information. Full details of experimental procedures for the synthesis of substances together with characterization data are provided in *SI Appendix*.

Data Availability. All study data are included in the article and/or *SI Appendix*.

ACKNOWLEDGMENTS. This research was supported by NSF Grant CHE-1954515 (to K.M.L.) and Department of Energy, Office of Science, Office of Basic Energy Sciences Grant DE-SC0017619 (to D.G.N.). The NSF also provided instrument support to the Department of Chemistry Instrumentation Facility at the Massachusetts Institute of Technology (MIT) (Grants CHE-9808061 and DBI-9729592). This work was supported in part by Robert Bosch LLC through its MIT Energy Initiative Sustaining Membership Agreement. This work was performed in part at the Harvard University Center for Nanoscale Systems; a member of the National Nanotechnology Coordinated Infrastructure Network, which is supported by the NSF under award no. ECCS-2025158. We thank Dr. Sarah S. Park and Dr. Adam J. Rieth for assistance with physical measurements and Dr. Miguel Gonzalez and Kay Xia for helpful comments. We additionally thank Prof. Yang Shao-Horn for her helpful advice on minimizing the fluorescence background of Raman spectra. XAS data were obtained at the Stanford Synchrotron Radiation Lightsource, which is supported by the US Department of Energy, Office of Science, Office of Basic Energy Sciences Contract DE-AC02-76SF00515. The SSRL Structural Molecular Biology Program is supported by the Department of Energy's Office of Biological and Environmental Research and by NIH/National Institute of General Medical Sciences (including Grant P41GM103393).

1. K. M. Abraham, Z. Jiang, A polymer electrolyte-based rechargeable lithium/oxygen battery. *J. Electrochem. Soc.* **143**, 1–5 (1996).
2. G. Girishkumar, B. McCloskey, A. C. Luntz, S. Swanson, W. Wilcke, Lithium-air battery: Promise and challenges. *J. Phys. Chem. Lett.* **1**, 2193–2203 (2010).
3. J. Christensen *et al.*, A critical review of Li/air batteries. *J. Electrochem. Soc.* **159**, R1–R30 (2011).
4. Y.-C. Lu *et al.*, Lithium-oxygen batteries: Bridging mechanistic understanding and battery performance. *Energy Environ. Sci.* **6**, 750–768 (2013).
5. D. Aurbach, B. D. McCloskey, L. F. Nazar, P. G. Bruce, Advances in understanding mechanisms underpinning lithium-air batteries. *Nat. Energy* **1**, 16128 (2016).
6. X. Yao, Q. Dong, Q. Cheng, D. Wang, Why do lithium-oxygen batteries fail: Parasitic chemical reactions and their synergistic effect. *Angew. Chem. Int. Ed. Engl.* **55**, 11344–11353 (2016).
7. D.G. Kwabi *et al.*, Materials challenges in rechargeable lithium-air batteries. *MRS Bull.* **39**, 443–452 (2014).
8. N. Mahne, O. Fontaine, M. O. Thotiyl, M. Wilkening, S. A. Freunberger, Mechanism and performance of lithium-oxygen batteries–A perspective. *Chem. Sci. (Camb.)* **8**, 6716–6729 (2017).
9. D. G. Kwabi *et al.*, Controlling solution-mediated reaction mechanisms of oxygen reduction using potential and solvent for aprotic lithium-oxygen batteries. *J. Phys. Chem. Lett.* **7**, 1204–1212 (2016).
10. C. M. Burke, V. Pande, A. Khetan, V. Viswanathan, B. D. McCloskey, Enhancing electrochemical intermediate solvation through electrolyte anion selection to increase nonaqueous Li-O_2 battery capacity. *Proc. Natl. Acad. Sci. U.S.A.* **112**, 9293–9298 (2015).
11. D. Sharon *et al.*, Catalytic behavior of lithium nitrate in Li-O_2 cells. *ACS Appl. Mater. Interfaces* **7**, 1659–16600 (2015).
12. K. U. Schwenke, M. Metzger, T. Restle, M. Piana, H. A. Gasteiger, The influence of water and protons on Li_2 O_2 crystal growth in aprotic Li-O_2 cells. *J. Electrochem. Soc.* **162**, A573–A584 (2015).
13. N. B. Aetukuri *et al.*, Solvating additives drive solution-mediated electrochemistry and enhance toroid growth in non-aqueous Li-O_2 batteries. *Nat. Chem.* **7**, 50–56 (2015).
14. D. G. Kwabi *et al.*, Chemical instability of dimethyl sulfoxide in lithium-air batteries. *J. Phys. Chem. Lett.* **5**, 2850–2856 (2014).
15. S. A. Freunberger *et al.*, Reactions in the rechargeable lithium-O_2 battery with alkyl carbonate electrolytes. *J. Am. Chem. Soc.* **133**, 8040–8047 (2011).
16. Y. Chen, S. A. Freunberger, Z. Peng, F. Bardé, P. G. Bruce, Li-O_2 battery with a dimethylformamide electrolyte. *J. Am. Chem. Soc.* **134**, 7952–7957 (2012).
17. A. Khetan, H. Pitsch, V. Viswanathan, Solvent degradation in nonaqueous Li-O_2batteries: Oxidative stability versus H-abstraction. *J. Phys. Chem. Lett.* **5**, 2419–2424 (2014).
18. J. M. García, H. W. Horn, J. E. Rice, Dominant decomposition pathways for ethereal solvents in Li-O_2batteries. *J. Phys. Chem. Lett.* **6**, 1795–1799 (2015).
19. E. Mourad *et al.*, Singlet oxygen from cation driven superoxide disproportionation and consequences for aprotic metal-O_2 batteries. *Energy Environ. Sci.* **12**, 2559–2568 (2019).
20. Y. Wang, Y.-R. Lu, C.-L. Dong, Y.-C. Lu, Critical factors controlling superoxide reactions in lithium-oxygen batteries. *ACS Energy Lett.* **5**, 1355–1363 (2020).
21. M. D. Radin, D. J. Siegel, Charge transport in lithium peroxide: Relevance for rechargeable metal-air batteries. *Energy Environ. Sci.* **6**, 2370–2379 (2013).
22. K. C. Lau, J. Lu, X. Luo, L. A. Curtiss, K. Amine, Implications of the unpaired spins in Li-O_2 battery chemistry and electrochemistry: A minireview. *ChemPlusChem* **80**, 336–343 (2015).
23. L. Andrews, Matrix infrared spectrum and bonding in the lithium superoxide molecule, LiO_2. *J. Am. Chem. Soc.* **90**, 7368–7370 (1968).
24. L. Andrews, Infrared spectrum, structure, vibrational potential function, and bonding in the lithium superoxide molecule LiO_2. *J. Chem. Phys.* **50**, 4288–4299 (1969).
25. L. Andrews, Ultraviolet absorption studies of the alkali metal atom-oxygen molecule matrix reaction. *J. Mol. Spectrosc.* **61**, 337–345 (1976).

26. D. M. Lindsay, D. A. Garland, ESR spectra of matrix-isolated lithium superoxide. *J. Phys. Chem.* **91**, 6158–6161 (1987).
27. X. Wang, L. Andrews, Infrared spectra, structure and bonding in the LiO_2, LiO_2Li, LiO and Li_2O molecules in solid neon. *Mol. Phys.* **107**, 739–748 (2009).
28. I. I. Vol'nov, S. A. Tokareva, V. N. Belevskii, V. I. Klimanov, Investigation of the nature of the interaction of lithium peroxide with ozone. *Russ. Chem. Bull.* **16**, 1369–1371 (1967).
29. X. Zhang *et al.*, LiO_2: Cryosynthesis and chemical/electrochemical reactivities. *J. Phys. Chem. Lett.* **8**, 2334–2338 (2017).
30. J. Lu *et al.*, A lithium-oxygen battery based on lithium superoxide. *Nature* **529**, 377–382 (2016).
31. J. Yang *et al.*, Evidence for lithium superoxide-like species in the discharge product of a Li-O_2 battery. *Phys. Chem. Chem. Phys.* **15**, 3764–3771 (2013).
32. F. S. Gittleson *et al.*, Raman spectroscopy in lithium-oxygen battery systems. *ChemElectroChem* **2**, 1446–1457 (2015).
33. J. K. Papp *et al.*, Poly(vinylidene fluoride) (PVDF) binder degradation in Li_2O_2batteries: A consideration for the characterization of lithium superoxide. *J. Phys. Chem. Lett.* **8**, 1169–1174 (2017).
34. A. Halder *et al.*, Identification and implications of lithium superoxide in Li-O_2 batteries. *ACS Energy Lett.* **3**, 1105–1109 (2018).
35. W.-J. Kwak, J.-B. Park, H.-G. Jung, Y.-K. Sun, Controversial topics on lithium superoxide in Li-O_2 batteries. *ACS Energy Lett.* **2**, 2756–2760 (2017).
36. C. G. de Kruif, E. J. Smit, H. A. J. Govers, Thermodynamic properties of 1,4-benzoquinone (BQ), 1,4-hydroquinone (HQ), 1,4-naphthoquinone (NQ), 1,4-naphthohydroquinone (NHQ), and the complexes BQ-HQ 1:1, NQ-HQ 1:1, NQ-NHQ 2:1, and NQ-NHQ 1:1. *J. Chem. Phys.* **74**, 5838–5841 (1981).
37. H. G. Kuivila, Electrophilic displacement reactions. III. Kinetics of the reaction between hydrogen peroxide and benzeneboronic acid. *J. Am. Chem. Soc.* **76**, 870–874 (1954).
38. J.-M. Lü, S. V. Rosokha, J. K. Kochi, Stable (long-bonded) dimers via the quantitative self-association of different cationic, anionic, and uncharged pi-radicals: Structures, energetics, and optical transitions. *J. Am. Chem. Soc.* **125**, 12161–12171 (2003).
39. S. V. Rosokha, J. Lu, T. Y. Rosokha, J. K. Kochi, Counter-ion modulation of long-distance pi-bonding of the open-shell *p*-benzoquinone anions. *Phys. Chem. Chem. Phys.* **11**, 324–332 (2009).
40. Z. Song, Y. Qian, T. Zhang, M. Otani, H. Zhou, Poly(benzoquinonyl sulfide) as a high-energy organic cathode for rechargeable Li and Na batteries. *Adv. Sci. (Weinh.)* **2**, 1500124 (2015).
41. L. Johnson *et al.*, The role of LiO_2solubility in O_2reduction in aprotic solvents and its consequences for Li-O_2batteries. *Nat. Chem.* **6**, 1091–1099 (2014).
42. H. Gampp, S. J. Lippard, Reinvestigation of 18-crown-6 ether/potassium superoxide solutions in Me_2SO. *Inorg. Chem.* **22**, 357–358 (1983).
43. A. Desbéne-Monvernay, P. C. Lacaze, A. Cherigui, UV-visible spectroelectrochemical study of some para- and ortho-benzoquinoid compounds: Comparative evaluation of their electrochromic properties. *J. Electroanal. Chem. Interfac.* **260**, 75–90 (1989).
44. Y. Matsunaga, The electron spin resonance absorption spectra of some semiquinone ions: Part III. Free radical salts of quinhydrones. *Can. J. Chem.* **38**, 1172–1176 (1960).
45. A. U. Khan, S. D. Mahanti, Collective electron effects of O_2^- in potassium superoxide. *J. Chem. Phys.* **63**, 2271–2278 (1975).
46. J. D. Cyran, J. M. Nite, A. T. Krummel, Characterizing anharmonic vibrational modes of quinones with two-dimensional infrared spectroscopy. *J. Phys. Chem. B* **119**, 8917–8925 (2015).
47. X. Zhao *et al.*, Resonance Raman and FTIR spectra of isotope-labeled reduced 1,4-benzoquinone and its protonated forms in solutions. *J. Phys. Chem.* **101**, 622 (1997).
48. S. C. B. Myneni, Soft X-ray spectroscopy and spectromicroscopy studies of organic molecules in the environment. *Rev. Mineral. Geochem.* **49**, 485–579 (2002).
49. J. T. Francis, A. P. Hitchcock, Inner-shell spectroscopy of *p*-benzoquinone, hydroquinone, and phenol: Distinguishing quinoid and benzenoid structures. *J. Phys. Chem.* **96**, 6598–6610 (1992).
50. U. Couhorn, R. Dronskowski, Alkali metal compounds of hydroquinone: Synthesis and crystal structure. *Z. Anorg. Allg. Chem.* **629**, 647–652 (2003).
51. A. R. Lippert, G. C. Van de Bittner, C. J. Chang, Boronate oxidation as a bioorthogonal reaction approach for studying the chemistry of hydrogen peroxide in living systems. *Acc. Chem. Res.* **44**, 793–804 (2011).
52. B. Kalyanaraman, M. Hardy, R. Podsiadly, G. Cheng, J. Zielonka, Recent developments in detection of superoxide radical anion and hydrogen peroxide: Opportunities, challenges, and implications in redox signaling. *Arch. Biochem. Biophys.* **617**, 38–47 (2017).
53. Y. Che *et al.*, Water-induced disproportionation of superoxide ion in aprotic solvents. *J. Phys. Chem.* **100**, 20134–20137 (1996).
54. K. Piech, T. Bally, T. Ichino, J. Stanton, Vibronic spectra of the *p*-benzoquinone radical anion and cation: A matrix isolation and computational study. *Phys. Chem. Chem. Phys.* **16**, 2011–2019 (2014).
55. A. R. Cook, L. A. Curtiss, J. R. Miller, Fluorescence of the 1,4-benzoquinone radical anion. *J. Am. Chem. Soc.* **119**, 5729–5734 (1997).
56. J.-M. Lü, S. V. Rosokha, I. S. Neretin, J. K. Kochi, Quinones as electron acceptors. X-ray structures, spectral (EPR, UV-vis) characteristics and electron-transfer reactivities of their reduced anion radicals as separated vs contact ion pairs. *J. Am. Chem. Soc.* **128**, 16708–16719 (2006).
57. E. A. C. Lucken, 814. Ion-association and specific solvation in the electron spin resonance spectra of semiquinones. *J. Chem. Soc.*, 10.1039/JR9640004234 (1964).
58. M. Yashiro, K. Sato, A new electrochromic material: 1,4-Benzoquinone in a non-aqueous solution. *Jpn. J. Appl. Phys.* **20**, 1319 (1981).
59. K. J. Stutts, G. W. Eastland, The lithium salt of benzoquinone radical anion and voltammetric anomalies. *J. Electroanal. Chem. Interfacial Electrochem.* **235**, 357–359 (1987).
60. M. A. Brown, B. R. McGarvey, D. G. Tuck, Structure of lithium-*p*-semiquinonates in non-aqueous solutions. *J. Chem. Soc., Dalton Trans.*1371–1376 (1998).
61. X. Zhao, T. Kitagawa, Solvent effects of 1,4-benzoquinone and its anion radicals probed by resonance Raman and absorption spectra and their correlation with redox potentials. *J. Raman Spectrosc.* **29**, 773–780 (1998).
62. G. Czapski, L. M. Dorfman, Pulse radiolysis studies. V. Transient spectra and rate constants in oxygenated aqueous solutions. *J. Phys. Chem.* **68**, 1169–1177 (1964).
63. I. B. C. Matheson, J. Lee, The absorption spectrum of superoxide anion in dimethylsulfoxide. *Spectrosc. Lett.* **2**, 117–119 (1969).
64. N. Seriani, *Ab initio* thermodynamics of lithium oxides: From bulk phases to nanoparticles. *Nanotechnology* **20**, 445703 (2009).
65. K. C. Lau, L. A. Curtiss, J. Greeley, Density functional investigation of the thermodynamic stability of lithium oxide bulk crystalline structures as a function of oxygen pressure. *J. Phys. Chem. C* **115**, 23625–23633 (2011).
66. D. Zhai *et al.*, Interfacial effects on lithium superoxide disproportionation in Li-O_2 batteries. *Nano Lett.* **15**, 1041–1046 (2015).
67. M. W. Ruckman *et al.*, Interpreting the near edges of $O_2$and O_2^{-1}in alkali-metal superoxides. *Phys. Rev. Lett.* **67**, 2533–2536 (1991).
68. M. J. Welland *et al.*, An atomistically informed mesoscale model for growth and coarsening during discharge in lithium-oxygen batteries. *J. Chem. Phys.* **143**, 224113 (2015).
69. Y.-C. Lu, Y. Shao-Horn, Probing the reaction kinetics of the charge reactions of nonaqueous Li-O_2batteries. *J. Phys. Chem. Lett.* **4**, 93–99 (2013).
70. D. Zhai *et al.*, Raman evidence for late stage disproportionation in a Li-O_2battery. *J. Phys. Chem. Lett.* **5**, 2705–2710 (2014).
71. D. Bijl, H. Kainer, A. C. Rose-Innes, Stabilization of free radicals by adsorption: Detection by paramagnetic resonance. *Nature* **174**, 830–831 (1954).
72. S. T. Plunkett *et al.*, Charge transport properties of lithium superoxide in Li-O_2 batteries. *ACS Appl. Energy Mater.* **3**, 12575–12583 (2020).
73. B. Lee *et al.*, Theoretical evidence for low charging overpotentials of superoxide discharge products in metal-oxygen batteries. *Chem. Mater.* **27**, 8406–8413 (2015).
74. S. Li, J. Liu, B. Liu, First-principles study of the charge transport mechanisms in lithium superoxide. *Chem. Mater.* **29**, 2202–2210 (2017).
75. N. R. Mathiesen, S. Yang, J. M. García-Lastra, T. Vegge, D. J. Siegel, Charge transport in alkali-metal superoxides: A systematic first-principles study. *Chem. Mater.* **31**, 9156–9167 (2019).
76. Y. Zhang *et al.*, High-capacity and high-rate discharging of a Coenzyme Q10-catalyzed Li-O_2 battery. *Adv. Mater.* **30**, 1705571 (2018).
77. X. Gao, Y. Chen, L. Johnson, P. G. Bruce, Promoting solution phase discharge in Li-O_2 batteries containing weakly solvating electrolyte solutions. *Nat. Mater.* **15**, 882–888 (2016).
78. Z.-Z. Shen *et al.*, Revealing the surface effect of the soluble catalyst on oxygen reduction/evolution in Li-O_2batteries. *J. Am. Chem. Soc.* **141**, 6900–6905 (2019).
79. S. Matsuda, K. Hashimoto, S. Nakanishi, Efficient Li_2O_2 formation via aprotic oxygen reduction reaction mediated by quinone derivatives. *J. Phys. Chem. C* **118**, 18397–18400 (2014).
80. P. Zhang *et al.*, Promoting surface-mediated oxygen reduction reaction of solid catalysts in metal-O_2batteries by capturing superoxide species. *J. Am. Chem. Soc.* **141**, 6263–6270 (2019).
81. S. A. Freunberger *et al.*, The lithium-oxygen battery with ether-based electrolytes. *Angew. Chem. Int. Ed. Engl.* **50**, 8609–8613 (2011).
82. M. Balaish, A. Kraytsberg, Y. Ein-Eli, A critical review on lithium-air battery electrolytes. *Phys. Chem. Chem. Phys.* **16**, 2801–2822 (2014).
83. T. Liu *et al.*, Current challenges and routes forward for nonaqueous lithium-air batteries. *Chem. Rev.* **120**, 6558–6625 (2020).